Synthesis and Structural Characterization of Silica Dispersed Copper Nanomaterials with Unusual Thermal Stability Prepared by Precipitation−Gel Method

ARTICLE *in* THE JOURNAL OF PHYSICAL CHEMISTRY C · SEPTEMBER 2010

Impact Factor: 4.77 · DOI: 10.1021/jp101136x

6 AUTHORS, INCLUDING:

Zhiwei Huang
Chinese Academy of Sciences
15 PUBLICATIONS **362** CITATIONS

SEE PROFILE

Synthesis and Structural Characterization of Silica Dispersed Copper Nanomaterials with Unusual Thermal Stability Prepared by Precipitation-Gel Method

Zhiwei Huang,[†] Fang Cui,[†] Jingjing Xue,[†,‡] Jianliang Zuo,[†,‡] Jing Chen,*[,†] and Chungu Xia*[,†]

State Key Laboratory for Oxo Synthesis and Selective Oxidation, Lanzhou Institute of Chemical Physics, Chinese Academy of Sciences, Lanzhou 730000, China, and Graduate University of Chinese Academy of Sciences, Beijing 100039, China

Received: February 5, 2010; Revised Manuscript Received: June 24, 2010

Silica dispersed copper nanomaterials with high dispersion and unusual thermal stability were prepared by a simple precipitation-gel method, and their physicochemical properties have been characterized by a variety of techniques including FTIR, XRD, XPS, TG-DSC, SEM, TEM, H_2-TPR, and N_2 adsorption. Both $Cu(OH)_2$ nanoparticles and amorphous copper phyllosilicate are confirmed to present in the dried samples, whereas CuO nanoparticles and undecomposed copper phyllosilicate are determined in the calcined samples. $Cu(OH)_2$ nanoparticles are prone to assemble to wire-like structure during sample preparation, and their structure can be well preserved after calcination and silica dispersed CuO nanowires were obtained. The preparation procedure of precipitation gel is favorable for the formation of copper phyllosilicate, which is rather stable and played a profound effect on both the structure and thermal stability of the samples. In addition, the high dispersion and the one-dimensional structure of copper also contribute to the high stability of the samples.

1. Introduction

Low-dimensional nanomaterials such as nanoparticles, nanowires, nanorods, etc. are attractive catalysts, due to their high surface areas and small sizes.[1−4] Nonetheless, most of the catalytic reactions are high-temperature processes, and if metal or metal oxide nanomaterials were solely used (without the protection of protective agents), they would readily aggregate to larger agglomerates. As is well-known, sintering of metal involves solid state diffusion, and the rate of sintering is an activated process with a diffusion coefficient that is strongly temperature-dependent and closely related to the so-called Hüttig temperature ($T_{Hüttig} = 0.3T_m$, where T_m represents the absolute melting point) and Tammann temperature ($T_{Tammann} = 0.5T_m$).[5−8] It is reported that surface diffusion becomes significant near the $T_{Hüttig}$, whereas with further increasing temperature to near the $T_{Tammann}$, volume diffusion starts, and bulk atoms tend to move, which leads to interparticle diffusion and therefore coalescence of metal particles.[8,9] In addition, when the particle sizes of metals decrease into nanorange, their melting points decrease drastically with decreasing particle size, leading to a much lower thermal stability. Therefore, the low thermal stability of metal nanoparticles would inevitably limit their applications.[8]

As a relatively inexpensive metal, copper has been widely used in the field of catalysis (e.g., steam reforming,[10,11] methanol synthesis,[12,13] ester hydrogenolysis,[14] hydrogenation and dehydrogenation of alcohols,[15−17] reduction of NOx,[18,19] oxidation of CO,[20] etc.). However, due to the low melting point (ca. 1356 K) and thus the low $T_{Hüttig}$ (ca. 451 K) and $T_{Tammann}$ (ca. 678 K) of copper, copper nanocatalysts are apt to sintering during the high-temperature reactions (e.g., steam reforming[10] and methanol synthesis[13]), which becomes one of the scientifically most important and challenging problems. For metals, their stability is reported to follow the order: Ag < Cu < Au < Pd < Fe < Ni < Co < Pt < Rh < Ru < Ir < Os < Re.[21] Thus, copper-based catalysts are suggested to operate at relatively low-temperatures, i.e., no higher than 573 K.[22] To obtain dispersed copper catalysts, a wide variety of methods including impregnation, ion-exchange, sol−gel, and (co)precipitation, are most commonly used. Nevertheless, it is often not suitable for the conventional methods such as impregnation, ion-exchange, and sol−gel to prepare catalysts with high efficiency and good stability, especially at higher loadings.[16,23]

In our previous work, we found that the precipitation-gel (PG) technique is a simple and convenient method for the preparation of silica-supported copper catalyst with high dispersion, promising catalytic activity and good stability.[24] In this work, Cu/SiO_2 nanomaterials with CuO loading in a wide range from 10 to 90 wt % were prepared by PG method, and their structure, morphology, composition, and thermal stability were studied by a variety of techniques, including FTIR, XRD, XPS, TEM, HRTEM, SEM, TG-DSC, N_2 adsorption, and H_2-TPR. Systematic characterization results showed that both $Cu(OH)_2$ nanoparticles and amorphous copper phyllosilicate are present in the dried samples, regardless of copper loading. In addition, the $Cu(OH)_2$ nanoparticles are prone to assemble to wire-like structure under highly basic and hot solution conditions; after calcination their structure is well preserved and silica dispersed CuO nanowires were obtained. To obtain catalysts with high stability, complicated fabrication procedures and/or complex catalyst compositions are generally required. Although stable metal/metal oxide catalysts can be obtained by lowering their metal contents, it often needs high metal loadings to provide sufficient active sites to achieve satisfactory catalytic activity.[13,25] Nevertheless, up to now, it is still a big challenge to obtain catalysts with high metal loading, especially at metal/metal oxide content >30 wt %, to exhibit high dispersion and good stability. Surprisingly, we found that the Cu/SiO_2 nanomaterials can be prepared with small crystallite size, reasonable large specific surface area and high stability at wide CuO contents by this

* To whom correspondence should be addressed. E-mail: chenj@lzb.ac.cn; cgxia@lzb.ac.cn. Fax: +86-931-4968129. Tel: +86-931-4968089.
[†] Lanzhou Institute of Chemical Physics, Chinese Academy of Sciences.
[‡] Graduate University of Chinese Academy of Sciences.

10.1021/jp101136x
Published on Web 09/14/2010

simple PG method at large scale, even with CuO loadings up to 90 wt %. Cu/SiO_2 materials with a low reduction temperature, a small particle size, and a poor crystallinity, which are responsible for the appearance of the finely dispersed active Cu^0 or CuO phases, are potentially attractive catalysts for a wide range of reactions mentioned above. In addition, high thermal stability is also a very important factor (even a decisive factor) for the implication of the materials as catalysts. The combined advantages of high dispersion, small crystallite sizes, and high thermal stability of the samples prepared by PG method make them promising materials for catalysts. Furthermore, the wire-like structure of the $Cu(OH)_2$ in the dried samples and CuO in the calcined samples with high CuO loadings may also have relevant biological,[26,27] photoelectrical,[28,29] and magnetic[30] implications.

2. Experimental Section

Materials Fabrication. The silica dispersed copper nanomaterials with final copper oxide loading in the range of 10−90 wt % were prepared by a precipitation-gel (PG) method as described in our previous report.[24] Briefly, 30.0 g of $Cu(NO_3)_2 \cdot 3H_2O$ (AR.) was dissolved in 250 mL of deionized water, and then 67 mL of aqueous solution of NaOH (4 mol L^{-1}) was added to form a precipitate (pH >11). Next, the requisite amount of colloidal aqueous silica solution (SiO_2, 40.0 wt %, ammonium stabilized type, pH 9−9.5, $d \approx 24$ nm, Guangzhou Renmin Chemical Plant, China) was added to the solution of the precipitate to stabilize the microparticles of the precipitate and simultaneously form a gel due to the change of the pH of the silica sol. The amount of silica sol to be added is calculated by the amount of SiO_2 in the CuO/SiO_2 materials to be produced based on CuO content/the content of SiO_2 in the sol. The gel was then aged at 370−373 K for 4 h, followed by filtration and washing with hot distilled water. The obtained solid was dried at 393 K overnight to obtain the dried samples. Unless otherwise noted, the calcined samples were referred to the dried samples stepwise calcined at 723 K under air for 3 h. The final calcined samples were designated as PG*w*, where *w* denotes the nominal CuO loading of the samples. The practical CuO contents of the materials prepared above were measured by XRF (PANalytical Maglx PW 2403). For comparison, pure CuO was obtained by the same procedures as those of PG samples, except for not adding colloidal silica particles; after aging at 370−373 K, blue $Cu(OH)_2$ was transformed to black CuO. Pure $Cu(OH)_2$ was prepared by the above precipitation process; for the sake of obtaining pure $Cu(OH)_2$, the precipitant was aged at a low temperature of 303 K for 4 h, and after washing it was dried at room temperature. Pure SiO_2 was prepared by precipitating the colloidal aqueous silica solution mentioned above with NaOH (4 mol L^{-1}) and further treated as the above PG samples.

Characterization. Fourier transform infrared (FTIR) spectra were recorded at room temperature on powdered samples using the KBr wafer technique in a Nicolet Nexus 870 FTIR spectrometer. Spectra were recorded with a resolution of 4 cm^{-1}.

The X-ray powder diffraction (XRD) of the samples was carried out on a PANalytical X'pert Pro Diffractometer using nickel filtered Cu Kα radiation ($\lambda = 1.54178$ Å) with a scanning angle (2θ) of 10−80° and a voltage and current of 40 kV and 30 mA. For selected samples, patterns were obtained during in situ calcination in air up to 1073 K or reduction in 5% H_2/Ar at a flow rate of 50 mL min^{-1} up to 773 K. In these experiments the temperature was ramped between measurements at a rate of 10 K min^{-1} for in situ calcination or 5 K min^{-1} for in situ reduction with a 5-min pause at each temperature before recording the pattern. The crystallite sizes (d) of CuO and Cu in the samples were calculated by the Scherrer equation $d = k\lambda/\beta_L \cos\theta$, where k is the Debye−Scherrer constant (0.89), θ is the diffraction angle, and β_L is the full width at half-maximum introduced by grain size.[31] The average crystallite size of CuO was estimated from the average values at CuO(−111) ($2\theta = 35.5°$) and (111) ($2\theta = 38.8°$), and the average crystallite size of Cu^0 from the value at Cu (111) ($2\theta = 43.3°$). The diffraction lines were fitted by a pseudo-Voigt function, and the crystallite size corresponding to the broadening was determined from the Lorentzian part, and the microstrain was determined from the Gaussian part of the individual profile functions.[32,33]

Simultaneous TG/DSC experiments were performed on a Netzsch STA 449 F3 Jupiter in the temperature range 303−1273 K in N_2 atmosphere at a temperature ramp of 10 K min^{-1}. X-ray photoelectron spectra (XPS) were obtained using a VG ESCALAB 210 spectrometer equipped with a Mg Kα X-ray radiation source ($h\nu = 1253.6$ eV) and a hemispherical electron analyzer. The spectra were recorded in the constant pass energy mode with a value of 20 eV and all binding energies were calibrated using the Si2p peak at 103.4 eV as the reference.

Temperature-programmed reduction (TPR) measurements were carried out in a quartz U-tube reactor with 20 mg of sample used for each measurement. Prior to the reduction, the sample was pretreated at 473 K under He flow for 1 h. After cooling to room temperature, the sample was reduced with 5% H_2 in Ar at a flow rate of 50 mL min^{-1} and the temperature was increased to 773 K at a ramping rate of 10 K min^{-1}. H_2 consumption was continuously monitored by a thermal conductivity detector (TCD).

The BET surface area measurements were performed on a Micromeritics ASAP 2010 instrument at liquid nitrogen temperature. Prior to measurements, the samples were degassed at 473 K overnight. The field-emission scanning electron microscopy (FE-SEM) images were recorded using a JSM-6701F instrument operated at an accelerating voltage of 5 kV. The samples were ultrasonically dispersed in ethanol, and one drop of the suspension was placed on a copper sample holder and sputter-coated with gold before analysis. Transmission electron microscopic (TEM) investigations were carried out using a JEM2010 electron microscope at 200 kV. The samples were ultrasonically dispersed in ethanol, and drops of the suspension were placed on a carbon-enhanced copper grid and then dried in air.

3. Results

Figure 1A shows the FTIR spectra of dried PG samples along with pure $Cu(OH)_2$ prepared by precipitation. At CuO loading below 50 wt %, the apparent absorption bands at approximately 1110, 800, and 470 cm^{-1} are assigned to the different vibration modes of the Si−O bonds in the amorphous SiO_2.[16,18] In addition, a weak band at around 690 cm^{-1} is attributed to the δ_{OH} vibration of the structural hydroxyl group of $Cu(OH)_2$.[34] With increasing CuO content up to 50 wt %, the absorption bands of amorphous SiO_2 greatly decreased and almost vanished at higher loadings; while a shoulder peak at around 1035 cm^{-1} on the low frequency side of the ν_{SiO} band of SiO_2 at 1110 cm^{-1}, which is characteristic of the presence of copper phyllosilicate (chrysocolla),[34] appeared and became prominent with further increasing final CuO loading up to 90 wt %. More evidence for the presence of this phase will be given below. The shoulder peak at 935 cm^{-1} presented in the dried samples with CuO loading beyond 50 wt % was associated with the δ_{OH} vibration of $Cu(OH)_2$.[34,35] Furthermore, with increasing Cu

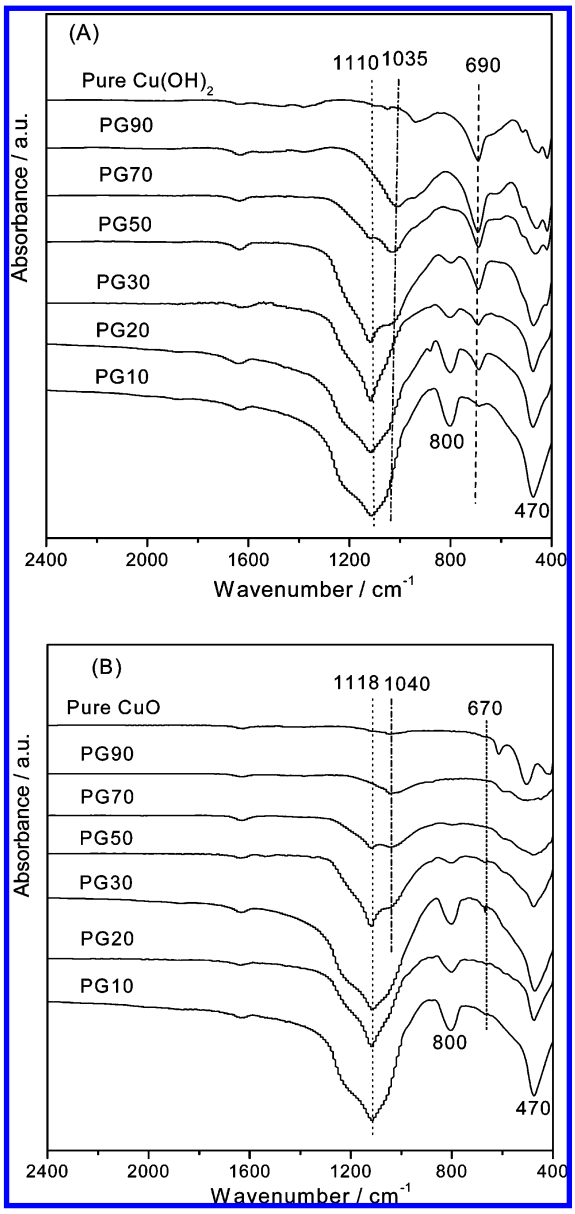

Figure 1. FTIR spectra of dried samples with their final CuO loading from 10−100 wt % (A) and calcined samples with copper oxide loading from 10−100 wt % (B).

content, the bands associated with the vibrations of Cu−O−H and Cu(II)-O species at low frequencies (<650 cm^{-1}) also became obvious.[35,36]

After calcination, as the spectra shown in Figure 1B, the absorption bands associated with $Cu(OH)_2$ totally disappeared, suggesting the completely decomposition of $Cu(OH)_2$ to CuO. In contrast, only slight decrease of the absorption of copper phyllosilicate located at approximately 1040 cm^{-1} for the high CuO containing samples was seen, implying that the structure of copper phyllosilicate was mainly reserved after calcination at 723 K. Our results are consistent with the previous reports that only partial decomposition of the copper phyllosilicate in catalysts prepared by ion exchange on rice husk ash[15] and nonporous silica[37] at 723 K was seen. Although the copper phyllosilicate in the calcined samples was largely preserved, only discernible characteristic δ_{OH} band of which at around 670 cm^{-1} was seen after the absence of the δ_{OH} band at 690 cm^{-1} from $Cu(OH)_2$.[34] In addition, with the vanishing of the broad band at 470 cm^{-1} from the support due to the drop of silica content, the characteristic vibrations of Cu−O bond in monoclinic CuO which appear at around 420, 500, and 610 cm^{-1} became more and more apparent.[38]

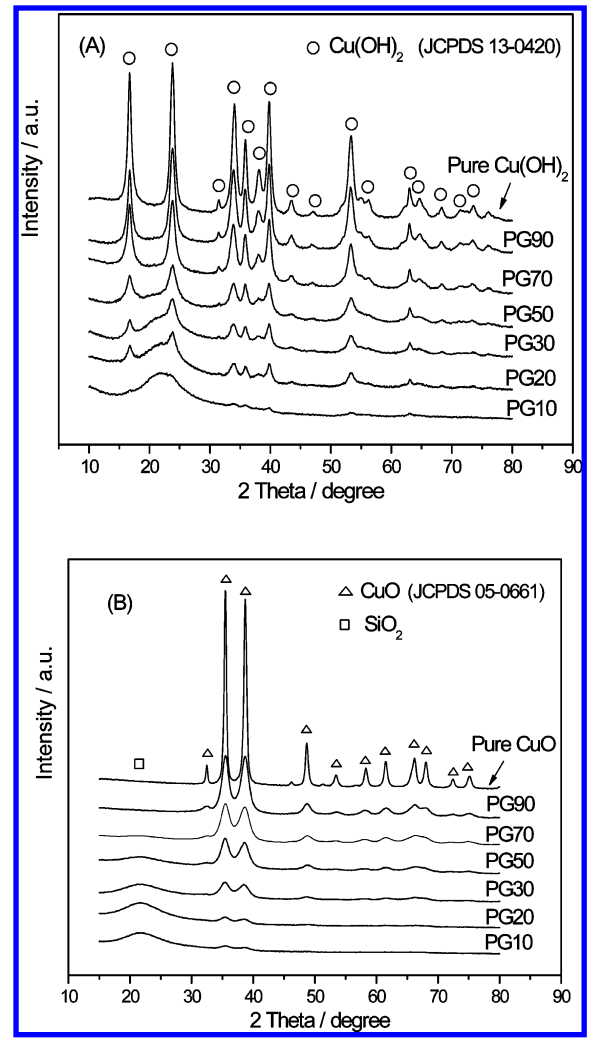

Figure 2. XRD profiles of the dried samples with their final CuO loading from 10−100 wt % (A) and calcined samples with copper oxide loading from 10−100 wt % (B).

Figure 2A presents the XRD patterns of the dried precursors of the samples with different copper loadings. For PG10 sample, the apparent feature was the broad diffraction peak at 2 θ around 22° due to amorphous silica; other diffuse but discernible diffraction peaks could be indexed to orthorhombic $Cu(OH)_2$. With increasing copper content, the intensity of the diffraction patterns of $Cu(OH)_2$ generally increased; and at the same time, the feature of amorphous silica smoothly weakened and almost vanished at CuO loading above 50 wt %. During the aging process, pure $Cu(OH)_2$ was easily transformed to CuO, and it is difficult to obtain pure $Cu(OH)_2$ at aging temperatures above 323 K. In the cases of silica containing PG samples (aged at 373 K and dried at 393 K), however, no characteristic XRD peaks arising from possible impurity such as CuO are detected, suggesting the high stability of the nanostructured $Cu(OH)_2$ in the dried Cu/SiO_2 samples.

After calcination, as the XRD patterns shown in Figure 2B, the $Cu(OH)_2$ in the dried precursors is completely transformed to monoclinic CuO. The intensities of the diffraction peaks of CuO gradually intensified with increasing copper content, suggesting the increasing crystallinity of the samples. Compared to pure CuO, however, the diffraction peaks of CuO of PG samples with CuO content even up to 90 wt % are rather broad and low, revealing the high dispersion and small crystallite sizes

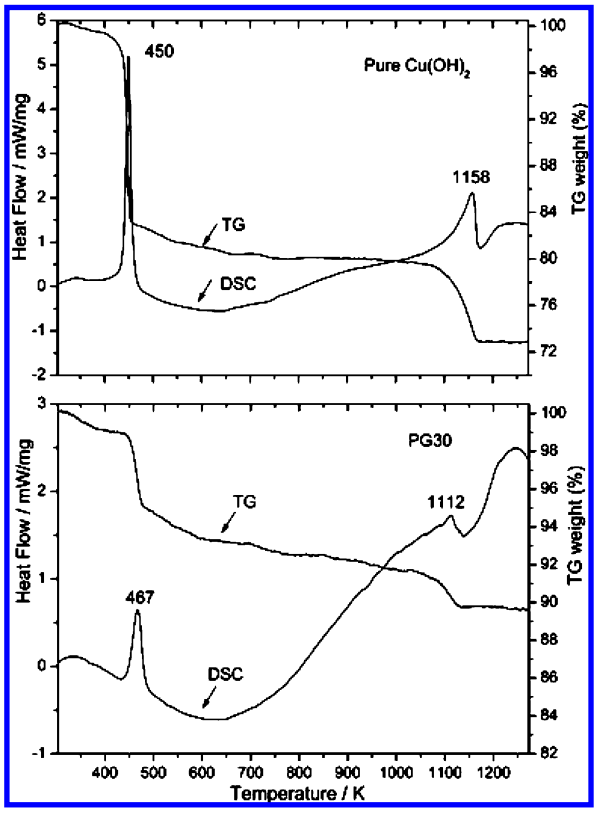

Figure 3. TG-DSC analysis of the dried PG30 sample and pure $Cu(OH)_2$.

of CuO in these samples. The mean crystallite sizes of CuO of the PG samples (shown in detail later) were controlled in a narrow range from 5.0 to 7.7 nm when CuO loading increased from 10 to 90 wt %. Pure CuO showed a much large crystallite size of 22.4 nm, clearly showing the stabilizing effect of silica for CuO particles in the silica containing samples. It should be remarked here that no diffraction peaks of copper phyllosilicate were seen in both the dried and calcined samples, regardless of copper loading, suggesting the amorphous structure of this species in the samples.

Figure 3 shows the typical TG-DSC data of the representative PG30 sample and the reference, pure $Cu(OH)_2$. PG30 sample exhibited two major endothermic weight loss features at 467 and 1112 K, whereas the pure $Cu(OH)_2$ showed two main endothermic weight loss processes at 450 and 1158 K. According to the XRD analysis and weight loss calculations, the low temperature peak is associated with the decomposition of $Cu(OH)_2$ to CuO and the high-temperature peak marks the conversion of CuO to Cu_2O. The onset decomposition temperature as well as the maximum weight loss peak for $Cu(OH)_2$ in the dried PG30 sample shifted to high temperature region with 14−17 K as compared to pure $Cu(OH)_2$, suggesting the presence of silica particles in the PG30 sample could inhibit the decomposition of $Cu(OH)_2$. The high stability of $Cu(OH)_2$ in the dried PG samples is in agreement with the above XRD characterization. In contrast, the CuO in PG30 sample transformed to Cu_2O at much lower temperature than that of decomposition of pure CuO, probably as a result of the effect of the nanoscale size.[39]

In situ XRD diffraction patterns were taken during the calcination of dried PG30 and PG70 samples (Figure 4A,B), the samples with the silica support riched and copper riched, respectively. Both samples showed the decomposition of $Cu(OH)_2$ at temperature between 443−473 K, which is in agreement with the TG-DSC result. With further increasing temperature up to 1073 K, only slight increase of the diffraction peaks of CuO was seen. The mean crystallite sizes of CuO for both samples slightly increased with the increase of calcination temperature (Figure 4C); nonetheless, even at a high temperature of 1073 K, the crystallite sizes of both samples remain below 7 nm, showing the high thermal stability of the PG samples in a wide CuO loading range.

The texture properties of calcined PG samples and the references (pure SiO_2 and CuO) containing CuO content, BET surface areas, average pore diameters and average crystallite sizes are compiled in Table 1. The BET surface area of the samples generally elevated with increasing CuO loading up to 70 wt %, which showed a maximum surface area of 224 m^2 g^{-1}. For PG90 sample, its surface area is still as high as 171 m^2 g^{-1}. Note that the surface area of pure SiO_2 and CuO are merely 114 and 16 m^2 g^{-1}, respectively. Van der Grift et al.[40] reported that the BET surface area of the Cu/SiO_2 catalysts prepared by homogeneous deposition-precipitation method using urea hydrolysis increased with the increase of Cu loading, and ascribed it to the formation of filandrous copper phyllosilicate which enhanced the BET surface area. In the present work, the increased BET surface areas for the calcined CuO/SiO_2 samples as compared to pure SiO_2 support as well as the BET surface areas generally increased with CuO loading up to 70 wt % may also be ascribed to the presence of copper phyllosilicate in these samples, as corroborated by IR. Although due to the low surface area of the silica support, the surface areas for CuO/SiO_2 materials prepared by PG method are generally lower than those prepared by homogeneous deposition-precipitation,[14,40] sol−gel,[16,41] or even traditional impregnation method,[16] high surface areas were seldom seen over the CuO/SiO_2 materials prepared by these methods at CuO loading above 50 wt %. In addition, the average pore diameters of silica support and the calcined PG samples are in the range of 10.9−19.2 nm, whereas pure CuO showed a large value of 53.8 nm.

Figure 5 shows the comparison of the in situ X-ray diffraction patterns taken during the reduction of the representative calcined PG30 and PG70 samples. The reduction process of both samples proceeded through an intermediate of Cu_2O in the range of 448−523 K. It seems that the calcined PG70 sample is more difficult to be reduced to Cu^0 than is the calcined PG30 sample, as the diffraction pattern of Cu_2O just became prominent for the former after reduced up to 498 K, whereas the diffraction of Cu_2O in the latter sample almost completely disappeared after reduction to this temperature. Further increase of reduction temperature resulted in a continuous intensification of the diffraction peaks of metallic copper. However, no significant increase in the amplitude of the diffraction peaks of copper was seen, even up to 773 K for both samples.

Figure 5c presents the crystallite sizes of the samples as a function of reduction temperature. At temperatures below 623 K, the crystallite sizes of both samples could maintain at ca. 5.4 nm. Further increase temperature to 773 K resulted in a slight increase of the crystallite sizes in both samples, with PG30 sample a bit more stable, as a lower extent of sintering for this sample was seen as compared to PG70. Noteworthy, the crystallite size of PG70 remained below 9 nm even after reduction at 773 K for 3 h, showing obviously the high stability of the Cu/SiO_2 samples prepared by PG method toward sintering, even with high copper loadings.

Figure 6 shows the H_2-TPR profiles of the calcined samples with different CuO contents. Each PG samples showed an asymmetric main reduction peak, which generally increased

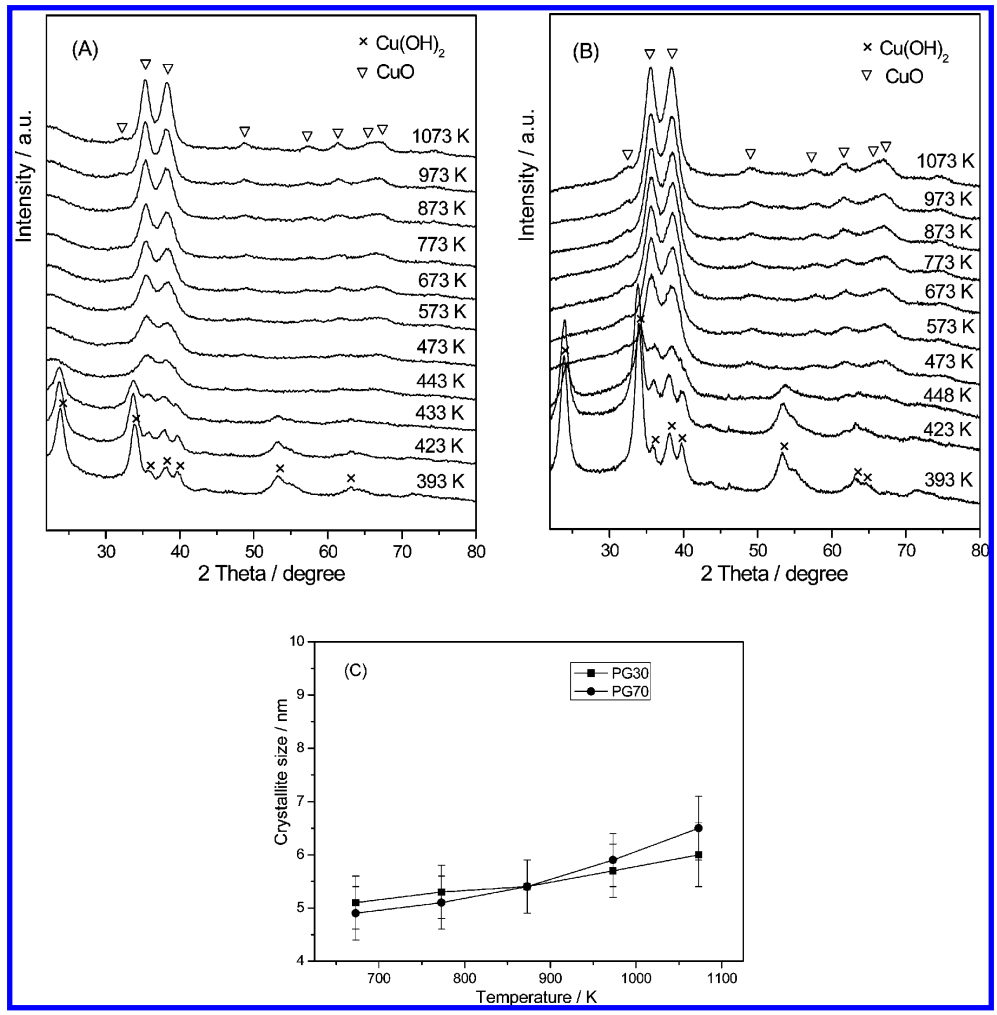

Figure 4. In situ X-ray diffraction during calcination of dried PG30 (A) and dried PG70 sample (B) in air in the range from 393 to 1073 K. (C) CuO crystallite sizes of PG30 and PG70 samples as a function of calcination temperature from 673 to 1073 K.

TABLE 1: Texture Properties of the Calcined Samples with Different CuO Contents

catalyst	CuO content[a] (wt %)	BET surface area[b] (m^2 g^{-1})	average pore diameter[c] (nm)	crystallite Size[d] (nm)
SiO_2	ND[e]	114	16.4	ND
PG10	10.9	167	12.9	5.0
PG20	21.3	158	14.3	5.2
PG30	31.6	186	13.0	5.5
PG50	53.4	203	11.8	5.7
PG70	70.5	224	10.9	6.4
PG90	90.3	171	19.2	7.7
pure CuO	ND	16	53.8	22.4

[a] Obtained from XRF analysis. [b] BET method. [c] BJH desorption average pore diameter. [d] Calculated from the Scherrer equation. [e] ND = not determined.

from 526 to 547 K with growing CuO loading from 10 to 70 wt %, and then profoundly decreased to 523 K with further increasing CuO content to 90 wt %. In addition, an attenuated peak at temperature approximately 35 K above each corresponding main peak presented in the samples with CuO loading in the range of 10−70 wt %, and almost vanished for PG90 sample. Differently, pure CuO showed a good symmetric hydrogen consumption peak centered around 506 K, which is 20−40 K lower than that of the silica containing samples. The onset reduction temperature of pure CuO was also much lower than that of the samples with high silica content (30−90 wt %), showing clearly the inhibiting effect of the silica particles in the reduction of Cu^{2+} species. Burattin et al.[42] reported the same inhibiting effect of silica in the reduction of nickel hydroxide. The difficulty in the reduction of PG70 sample in H_2-TPR as compared to that of PG30 sample is in good agreement with the in situ XRD results. Nonetheless, presently, it is hard to explain why the samples containing 50−70 wt % CuO are more difficult to be reduced to Cu^0, may be as a result of forming more hard-reducible copper phyllosilicate in these samples, as evidenced from BET surface area results.

On the basis of the FTIR and XRD results mentioned above and the XPS results as will be given below, we can see that there are generally two different copper species: dispersed CuO and copper phyllosilicate present in the calcined Cu/SiO_2 samples, while mainly bulk CuO present in the pure CuO. It is well-known that dispersed CuO with small particle sizes can be more easily reduced to Cu^0 than did the bulk CuO with larger sizes due to dynamic reasons.[43,44] In contrast, dispersed and surface interacted Cu^{2+} species are reported to be more difficult to reduce than bulk CuO.[45−47] The above-mentioned inhibiting effect of the silica particles in the reduction of the PG samples would probably be aroused by the presence of the surface interacted Cu^{2+} species, that is copper phyllosilicate in these samples. Chen et al.[14] reported that the main reduction peak of the Cu/SiO_2 catalysts prepared by ammonia evaporation is attributed to the collective contribution of the reduction of the well dispersed CuO to Cu^0 and the ion-exchanged Cu−O−Si and copper phyllosilicate to Cu^+, while the shoulder peak at high temperature is ascribed to the reduction of bulk CuO. The

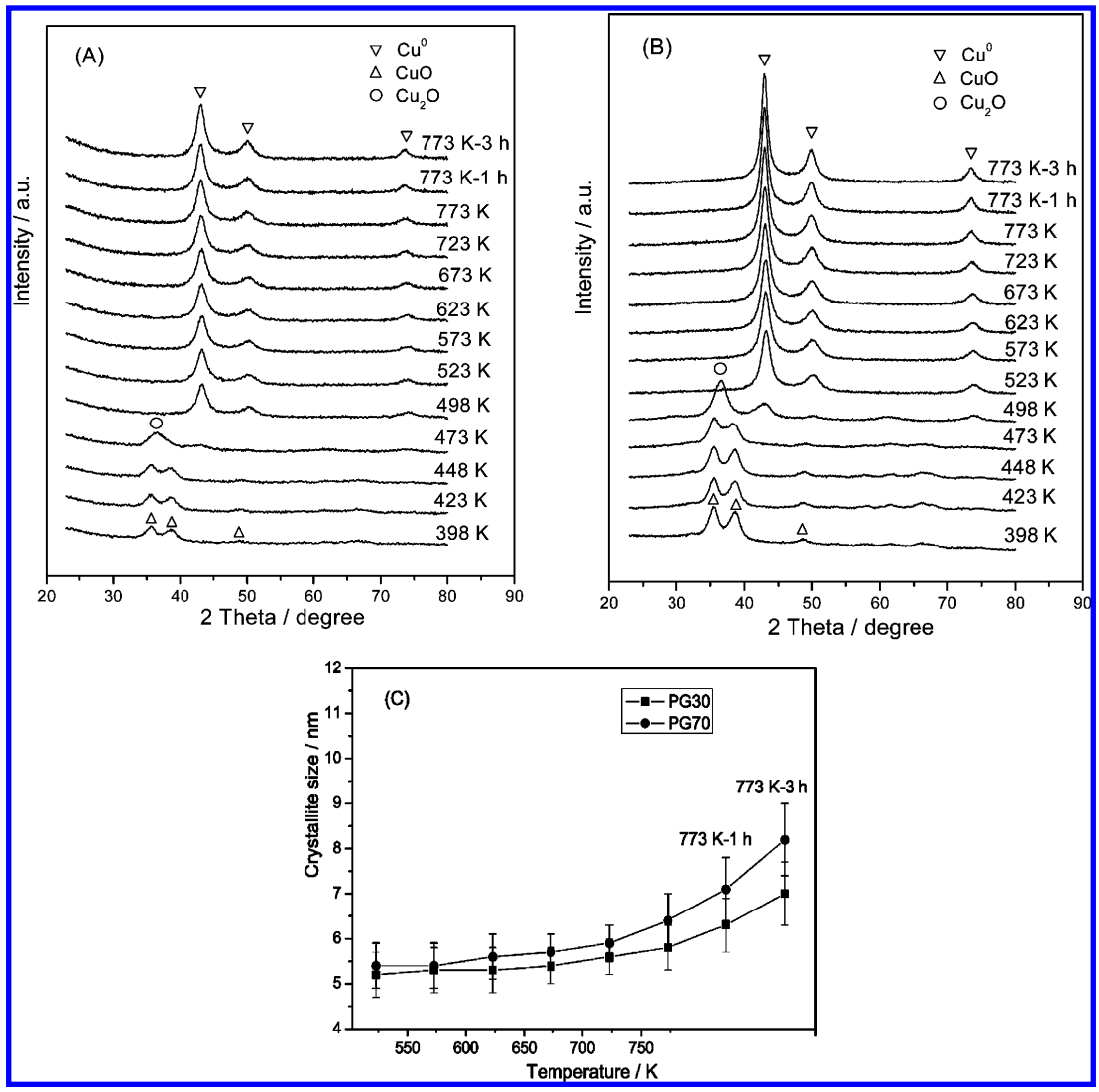

Figure 5. In situ XRD patterns taken during reduction of (a) calcined PG30 and (b) calcined PG70 and (c) Cu^0 crystallite sizes as a function of reduction temperature.

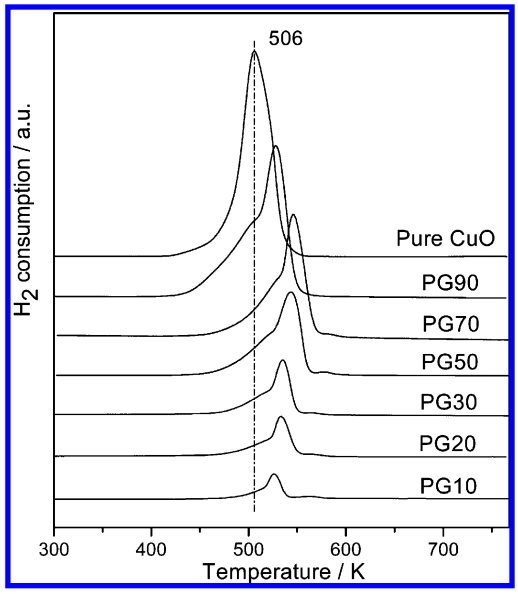

Figure 6. H_2-TPR profiles of the calcined PG samples with CuO loading from 10−90 wt % and the reference of pure CuO.

authors also ascribed the Cu^+ species highly interacted with the support to be reduced at temperature beyond 873 K. In our condition, since no other reduction peak was seen with the reduction temperature up to 973 K, it is reasonable that the main reduction peak of the CuO/SiO_2 samples is attributed to the collective contribution of stepwise reduction of dispersed CuO to Cu^0 (from in situ XRD results) and the partially reduction of supported copper phyllosilicate to Cu^+, whereas the shoulder peak in the high temperature range is ascribed to the reduction of supported Cu^+ (derived from the stepwise reduction of copper phyllosilicate) to Cu^0. It should be noted here that although there was no detection of the diffraction of Cu_2O after the in situ reduction of PG30 up to 498 K and PG70 up to 523 K, respectively, the presence of a small amount of Cu_2O, which is highly dispersed and undetectable by XRD but trackable by H_2-TPR, cannot be excluded.

The XP spectra of the calcined PG samples all showed a broad photoelectron peak at somewhat above 935.0 eV ($Cu2p_{3/2}$) with the silica riched samples (from PG10 to PG30) much higher, which are in the range of 935.6−935.8 eV. The high values of the BE along with the presence of the characteristic shakeup satellite peaks suggests that the copper oxidation state is +2 in all of these samples.[44] The BE of pure CuO prepared by precipitation was determined at 934.0 eV; thus, the relatively large positive BE shift of the Cu2p core level for the PG samples is indicative of a charge transfer from the metal ions toward

TABLE 2: Binding Energy and Surface and Bulk Atomic Ratios of the Calcined Samples

sample	position of $Cu2p_{3/2}$ (eV)	fwhm of $Cu2p_{3/2}$ (eV)	bulk Cu/Si ratio	XPS Cu/Si ratio
PG10	935.8	4.5	0.092	0.059
PG20	935.6	4.2	0.204	0.207
PG30	935.6	4.1	0.349	0.405
PG50	935.1	4.2	0.831	1.008
PG70	935.2	4.0	1.803	3.074
PG90	935.2	3.8	7.026	9.232
pure CuO	934.0	3.4		

the support matrix, that is, a strong interaction between the metal ions and the matrix.[48] Van der Gift et al.[40] found that no copper(II) oxide but copper phyllosilicate were present in the calcined CuO/SiO_2 samples prepared by homogeneous deposition-precipitation method using urea hydrolysis by XPS, as the BE of the latter is 2.0 eV higher than that of the former. In our condition, the high BE of the PG samples may also result from the formation of copper phyllosilicate, the presence of which can be detected by FTIR (Figure 1). The high fwhm of the $Cu2p_{3/2}$ spectra of the PG samples ($\geq$3.8 eV) also infers the presence of two kinds of Cu(II) species (CuO and copper phyllosilicate) in these samples. The XPS surface Cu/Si ratios of the samples increased with increasing CuO loading, and at CuO loading above 30 wt % the XPS surface Cu/Si ratios became larger than those of the bulk ratios (Table 2). These discrepancies suggest that with increasing CuO loading, copper species were gradually enriched on the surface of the PG samples.[49]

Figure 7 presents the SEM photographs of the calcined samples with different CuO loadings. As can be seen, the morphology of the products depends strongly on the content of CuO. At CuO content below 30 wt %, highly dispersed nanoparticles are the major products, and it is very difficult to discriminate between CuO nanoparticles and the silica supports. With increasing CuO loading, a few rod-like CuO particles are occasionally observed in PG30 sample, whereas abundant nanorods with diameter about 10−20 nm and lengths up to hundreds of nanometers, which are randomly dispersed by spherical silica particles, are present in the PG50 sample. At CuO loading above 50 wt %, nanorods are the major products, and their amount increases with increasing copper content. In addition, the nanorods tend to form some bundles larger than 100 nm in diameters with increasing CuO loading.

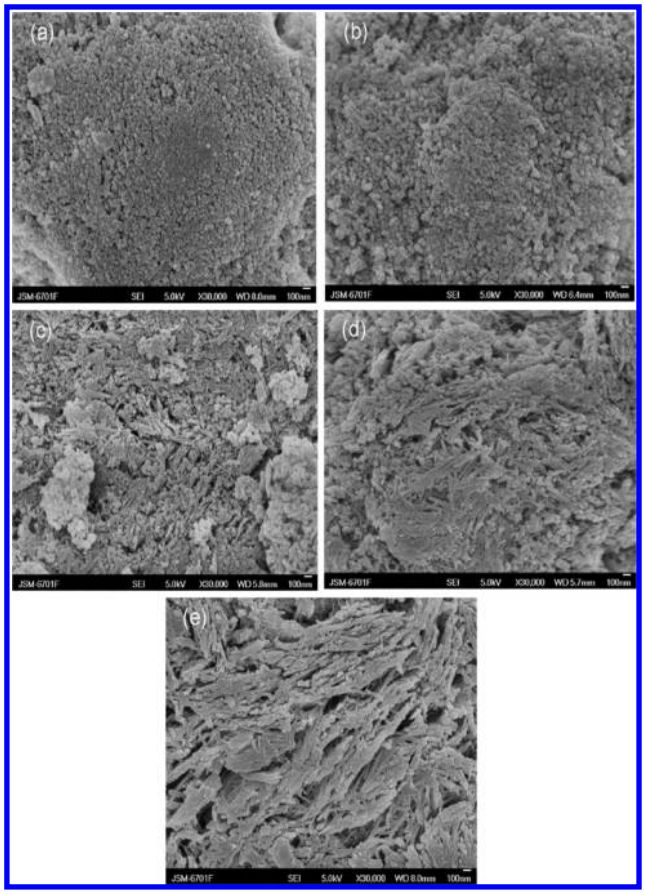

Figure 7. SEM photographs of the samples with different CuO contents: (a) PG10, (b) PG30, (c) PG50, (d) PG70, and (e) PG90.

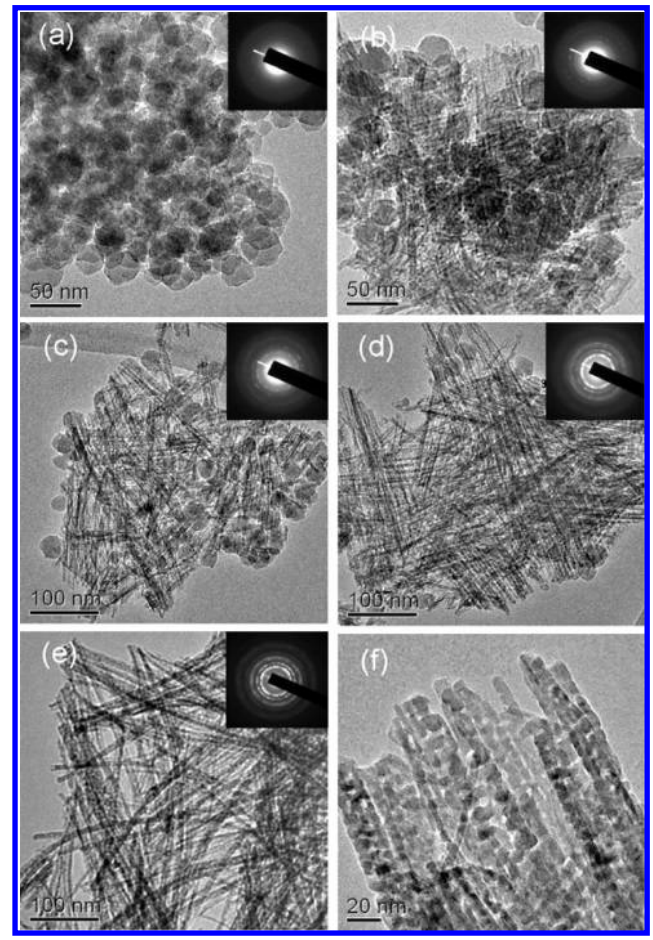

Figure 8. TEM images of the calcined samples with different CuO contents: (a) PG10, (b) PG30, (c) PG50, (d) PG70, and (e) PG90. (f) Higher magnification TEM image of bundled CuO nanowire of PG90 sample.

The typical TEM images of the calcined samples with different CuO loadings are presented in Figure 8. For calcined PG10 sample (Figure 8a), light gray spherical silica particles are identified along with highly dispersed dark one assignable to CuO particles. In addition, some filandrous structured materials due to the presence of copper phyllosilicate are also observed.[14] The inset of Figure 8a shows a corresponding select area electron diffraction (SAED) pattern, a few scattered spots are occasionally observed, characteristic of highly dispersed or amorphous samples with poor crystallinity. It should be remarked here that, besides the highly dispersed copper species indicated above, a few short nanowires with diameter of 2−6 nm and length up to several tens of nanometers are also observed in this sample. With increasing CuO loading, not only the amount but also the length of the nanowires increases (Figure

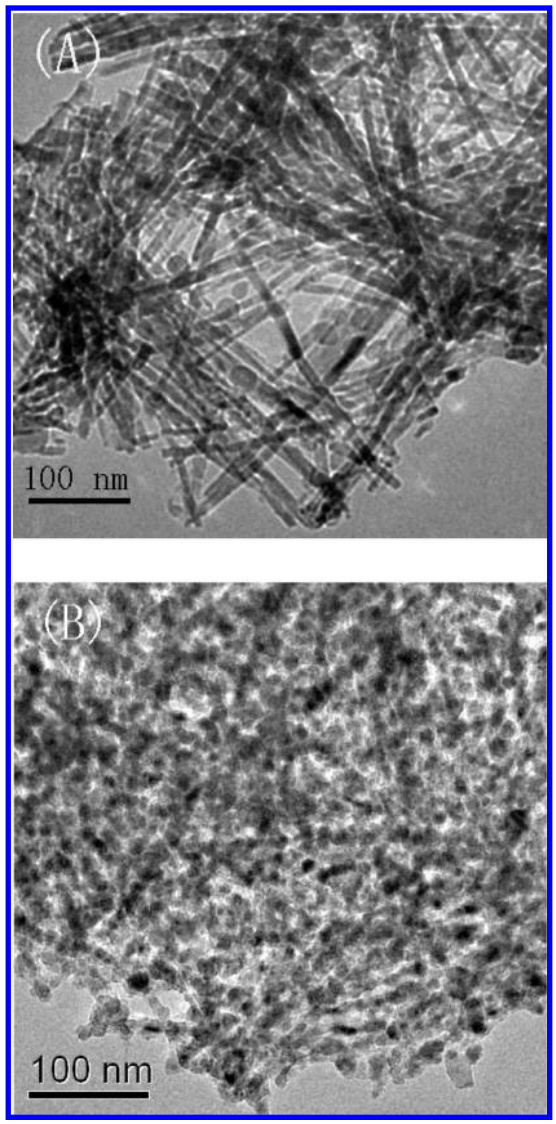

Figure 9. TEM images of dried PG70 sample calcined at 973 K for 3 h (A) and calcined (723 K) PG70 sample reduced at 773 K for 3 h.

8b−e), and nanowires with lengths up to several hundreds of nanometers are seen in the copper-rich PG70 and PG90 samples. However, almost no obvious increase of the beneath of the single nanowires was seen, as the average of which just increased from around 4 to 8 nm as the final copper oxide loading increased from 10 to 90 wt %. In addition, the nanowires are prone to assemble into wide bundles, especially in the samples with CuO loading above 50 wt %. These findings are in line with the SEM observations (Figure 7). The higher magnification TEM image of the bundled nanowires given in Figure 8f clearly showed that the nanowires are composed of coalesced nanoparticles, suggesting the final products are built from the original small nanocrystals by aggregation.

To study the stability as well as the morphologies of the PG samples during high temperature treatments, TEM images were also taken for both the dried PG70 sample calcined at 973 K for 3 h and the calcined (723 K) PG70 sample reduced at 773 K for 3 h (Figure 9). As can be seen, the rodlike morphology of the sample was well preserved after calcining at a relatively higher temperature, and only a slight increase of the average width of the CuO nanowires to around 9 nm was seen (Figure 9A). After reduction at 773 K, the nanowires in the calcined PG70 sample were largely decomposed to highly dispersed nanoparticles, and a proportion of nanoparticles composed of short nanorods with diameters of 4−14 nm can also be observed (Figure 9B). The average diameter of the nanorods is ca. 9 nm estimated from the TEM images and few large aggregates were seen. The above results apparently show the high stability of the samples during high temperature treatments, which are in agreement with the in situ XRD characterizations (Figures 4 and 5).

4. Discussion

4.1. Formation of Copper Phyllosilicate in the Dried and Calcined Samples. In our previous work,[24] we reported that it was $Cu(OH)_2$, not copper phyllosilicate, that was mainly present in the dried precursor of the Cu/SiO_2 catalyst with 30 wt % CuO loading prepared by PG method. From the above characterizations, we know that a proportion of copper phyllosilicate, which was not detectable by XRD and hardly by IR spectroscopy, were also present in the dried PG samples with CuO loading below 50 wt %. With the increase of CuO loading up to 50 wt %, due to the decrease in the amount of SiO_2 in the samples and also due to the consumption of silica to silicate, a band characteristic of the presence of copper phyllosilicate at around 1035 cm^{-1} in the IR spectrum can be distinguished. After calcination, IR spectra revealed that the structure of copper phyllosilicate in the dried samples was mainly reserved, whereas the $Cu(OH)_2$ species was fully decomposed to CuO. In addition, as mentioned above, the high BE of the $Cu2p_{3/2}$ and the wide fwhm of this peak in all calcined PG samples revealed the presence of copper phyllosilicate, besides CuO. Thus, all of the above results confirm that both CuO and copper phyllosilicate were indeed present in the calcined PG samples, regardless of CuO loading.

Copper phyllosilicate ($Cu_2Si_2O_5(OH)_2$), also called chrysocolla, is a kind of copper silicate with lamellar structure that consists of alternate layers of SiO_4 tetrahedra and discontinuous layers of CuO_6 octahedra. Copper phyllosilicate is known to form during the preparation of Cu/SiO_2 catalyst by the deposition-precipitation method using urea hydrolysis[40] or ammonia evaporation[14] and by selective adsorption of $[Cu(NH_3)_4]^{2+}$on SiO_2.[34] It is reported that there are two requirements for the aqueous solution formation of metal phyllosilicates: first the presence of OH bridging ligands in the neutral metal complex, which participate in heterocondensation reactions and second the presence of silicic acid, which is generated by dissolving of silica particles in a basic solution.[34,50] In the Cu/SiO_2 samples prepared by PG method, Cu^{2+} ions were first precipitated to $Cu(OH)_2$ microparticles, and then colloid silica nanoparticles, which are of high reactivity and would dissolve to form silicic acid during the following high pH aging process, were added therein to disperse and stabilize the previously formed $Cu(OH)_2$ nanoparticles. This preparation procedure fits very well with the above-mentioned requirements for the generation of metal phyllosilicates, thus explaining why copper phyllosilicate is present in all of the PG samples. It seems that the reactivity of the $Cu(OH)_2/SiO_2$ mixtures increases with increasing of $Cu(OH)_2$ content, as the BET surface area of the PG samples generally increased with increasing CuO loading up to 70 wt % and that of PG90 sample is also higher than the samples with CuO loading below 30 wt %. Furthermore, the high aging temperature (370−373 K) applied here are also favorable for the formation of copper phyllosilicate, as the generation of which is a kinetically limited process.[34]

4.2. Wire-Like Morphology of the Dried and Calcined Samples. The above SEM and TEM results have revealed that both nanoparticles and nanowires coexist in the Cu/SiO_2 samples

prepared by PG method, and with increasing CuO loading, not only the content but also the length of CuO nanowires in the samples generally increased. It is reported that $Cu(OH)_2$ nanomaterials are good precursors to prepare CuO nanomaterials with controlled morphologies.[51−54] Thus, the CuO nanowires in the calcined samples are inferred to derive from $Cu(OH)_2$ nanowires in the dried PG samples. The TEM investigation of the dried PG90 sample showed that this sample mainly composed of nanowires of 4−12 nm in width and up to several hundred nanometers in length, thus supporting the above deduction. Now comes one important question: why are these nanocrystals prepared by the PG method likely to assemble to wire-like structure instead of clusters or random particles?

As is well-known, $Cu(OH)_2$ is a layered material, and its orthorhombic crystal structure has been proven to be ideal for the assembly of one-dimensional (1D) nanomaterials.[27,35,53,55] According to the Bravais−Donnay−Harker (BDH) law, the crystal planes with larger d_{hkl} values grow more slowly; hence, the growth rate of $Cu(OH)_2$ nanowires along [100] direction is much faster than along other directions because of its lesser d_{hkl} value. In addition, Cu^{2+} prefers square-planar coordination by OH^- with strong σ_{x2-y2} bonds, forming a two-dimensional olated chains of [>$Cu(OH)_2$Cu<], which has proved to be critical for the formation of $Cu(OH)_2$ nanowires/nanoribbons.[27,52,55,56] In previous works, ammonia solutions were widely used to prepare $Cu(OH)_2$ nanowires by wet chemical method.[27,52,53,57] In these processes, NH_3 was first added to form a complex of $[Cu(NH_3)_n]^{2+}$ with Cu^{2+} ions, and then an aqueous hydroxyl solution of sodium or potassium was added to precipitate this complex to $Cu(OH)_2$ nanowires, in which NH_3 played a transporter role of Cu^{2+} ion.[27,52,53] It should be noted here that under a low NH_3/Cu^{2+} ratio and even in the absence of NH_3, $Cu(OH)_2$ nanowires were also facilely fabricated by directly precipitating Cu^{2+} ions with aqueous solution of NaOH or KOH.[27,58,59] During these processes, individual $Cu(OH)_2$ nanoparticles rather than long $Cu(OH)_2$ nanowires were formed at the beginning. Then $Cu(OH)_2$ nanowires grew preferentially by the oriented attachment of the primary nanoparticles, which was coupled with coordination self-assembly, resulting in polycrystalline $Cu(OH)_2$ nanowires.[27,30,36] In our preparation of Cu/SiO_2 samples by PG method, Cu^{2+} ions were first precipitated by aqueous solution of NaOH to form individual $Cu(OH)_2$ microparticles, then colloidal silica nanoparticles were added therein to disperse the previous formed $Cu(OH)_2$ nanoparticles. During the precipitation process as well as the dispersion and aging processes, the $Cu(OH)_2$ nanoparticles are likely to aggregate to longer nanocrystal-built polycrystalline $Cu(OH)_2$ nanowires by the above-mentioned oriented attachment and coordination self-assembly mechanisms.

In the TEM investigation of the calcined samples with different CuO loading, we have found that both the amount and the length of the CuO nanowires generally increase with elevating CuO loading. It seems that the presence of silica nanoparticles could inhibit the growing of $Cu(OH)_2$ nanocrystals to form elongated nanowires during the sample preparation. This inhibiting effect of SiO_2 particles can be interpreted as follows: on the one hand, during the sample preparation, colloidal silica nanoparticles were immediately added to the previously formed $Cu(OH)_2$ nanoparticles. Thus, the microparticles of $Cu(OH)_2$ did not have enough time to assemble to elongated nanowires before they were dispersed by large amount of silica nanoparticles. On the other hand, in a high pH aging condition, the surface of silica particles is negatively charged, whereas $Cu(OH)_2$ nanoparticles are positively charged,[58] which are likely to adsorb on the surface of silica particles and would further react with the −Si−OH to form copper phyllosilicate. Thus, mainly silica supported $Cu(OH)_2$ nanoparticles and copper phyllosilicate existed in the PG samples with low copper loadings. With increasing CuO loading, $Cu(OH)_2$ microparticles have more opportunity to attach together to form $Cu(OH)_2$ nanowires and longer $Cu(OH)_2$ nanowires with larger amount are formed, besides a small proportion of copper phyllosilicate.

4.3. Effect of the Structure and Morphology on the Stability of the Samples. It is common that the dispersion of a supported nanomaterial, e.g., catalyst, decreases monotonously with increasing loading, resulting in poor thermal stability. Therefore, it is often difficult to obtain catalysts and other supported nanomaterials with high metal loading, especially at metal/metal oxide content >30 wt %, to exhibit high dispersion and good stability. In our condition, however, samples with CuO loading even as high as 70 wt % exhibited unusual stability as the in situ XRD calcination and reduction of the representative samples shown in Figures 4 and 5. The mean crystallite size of CuO in the PG70 sample could maintain below 7 nm with calcination in air up to 1073 K, whereas the crystallite size of Cu^0 could remain below 9 nm with reduction in H_2 up to 773 K, even with reduction at this high temperature for 3 h. Note that the calcination temperature and reduction temperature are much higher than the corresponding $T_{Tammann}$ of CuO (ca. 800 K) and $T_{Tammann}$ of Cu^0 (ca. 678 K). Taking the above structure and morphology characterizations into consideration, the high stability of the samples prepared by PG method can be explained as follows:

On the one hand, as the XPS results compiled in Table 2, the surface Cu/Si ratios are very close to those of the bulk phase, especially at CuO loading below 50 wt %, showing the high dispersion of the samples.[11] In addition, the SEM and TEM images shown in Figures 7 and 8, respectively, also revealed the high dispersion of the samples. The high dispersion of the samples prepared by PG method may play an important role in their high stability. It is reported that the formation of layered copper phyllosilicate species played a key role in the obtention of Cu/SiO_2 samples prepared by cationic exchange with good stability.[34,37] The presence of copper phyllosilicate in our condition, on the other hand, might play the same key role in the unusual stability of the Cu/SiO_2 samples prepared by PG method. Furthermore, the 1D morphology of $Cu(OH)_2$ nanowires in the dried samples and CuO nanowires in the calcined samples, which had easier movement in the axial direction but more difficult movement in the radial direction, may also contribute to the high stability of the samples, as the TEM results shown in Figure 9.

5. Conclusions

Nanostructured Cu/SiO_2 materials with CuO loading in a wide range from 10 to 90 wt % have been fabricated by a simple precipitation-gel method. A variety of techniques, including FTIR, XRD, XPS, TG-DSC, TEM, SEM, N_2 adsorption, and H_2-TPR have been applied to characterize the structure, morphology, composition, and thermal stability of the samples. The primary conclusions of this study are summarized below.

(1) Both $Cu(OH)_2$ nanoparticles and copper phyllosilicate are determined to be present in the dried Cu/SiO_2 samples, regardless of copper content. $Cu(OH)_2$ nanoparticles are likely to assemble to wire-like structures, and not only the amount but also the length of $Cu(OH)_2$ nanowires in the dried samples can generally be tuned by the loading of copper, with the sample containing 90 wt % CuO having $Cu(OH)_2$ a narrow width of 4−12 nm and length up to several hundred nanometers.

(2) $Cu(OH)_2$ nanoparticles and nanowires can be easily transformed to CuO after calcination in the range of 423−473 K with their structure well preserved. In contrast, copper phyllosilicate in the dried samples is very stable with its structure largely reserved after calcination at 723 K. Therefore, both dispersed CuO and copper phyllosilicate coexist in the calcined PG samples, irrespective of copper loading.

(3) The reduction of dispersed CuO in the calcined PG samples to Cu^0, which underwent an intermediate of Cu_2O, is much harder than that of pure bulk CuO, probably due to the inhibiting effect of the presence of highly interacted Cu^{2+} species, i.e., copper phyllosilicate in these samples.

(4) The Cu/SiO_2 materials prepared by PG method exhibited unusual stability toward high temperature calcination and reduction, with the mean crystallite sizes of CuO in the samples calcined up to 1073 K and Cu^0 in the samples reduced up to 773 K could maintain below 9 nm, even with CuO loading up to above 70 wt %.

(5) The high stability of the materials can be ascribed to the high dispersion of the samples and the presence of a small amount of copper phyllosilicate in these samples. In addition, the 1D morphology of copper in the samples may also contribute to their high stability.

(6) The combined advantages of high dispersion, small crystallite size, and high thermal stability of the samples make them promising materials for catalysts. Moreover, the 1D nanostructures of the $Cu(OH)_2$ and CuO in the dried and calcined samples with high CuO loadings, respectively, may also have relevant biological, photoelectrical, and magnetic implications.

Acknowledgment. The authors gratefully acknowledge the technical assistance provided by Ms. L. He and Ms. L. Gao and the financial support from the National Science Fund for Distinguished Young Scholars of China (Grant 20625308) and the National Natural Science Foundation of China (Grant 20973187).

References and Notes

(1) Bell, A. T. *Science* **2003**, *299*, 1688–1691.
(2) Zheng, N.; Stucky, G. D. *J. Am. Chem. Soc.* **2006**, *128*, 14278–14280.
(3) Formo, E.; Lee, E.; Campbell, D.; Xia, Y. *Nano Lett.* **2008**, *8*, 668–672.
(4) Xie, X. W.; Li, Y.; Liu, Z. Q.; Haruta, M.; Shen, W. J. *Nature* **2009**, *458*, 746–749.
(5) Moulijn, J. A.; van Diepen, A. E.; Kapteijn, F. *Appl. Catal., A* **2001**, *212*, 3–16.
(6) Hüttig, G. F. *Arch. Metall.* **1948**, *2*, 93–99.
(7) Spencer, M. S. *Nature* **1986**, *323*, 685–687.
(8) Sun, J.; Ma, D.; Zhang, H.; Liu, X.; Han, X.; Bao, X.; Weinberg, G.; Pfander, N.; Su, D. *J. Am. Chem. Soc.* **2006**, *128*, 15756–15764.
(9) Menon, P. G.; Rao, T. *Catal. Rev.-Sci. Eng.* **1979**, *20*, 97–120.
(10) Matter, P. H.; Braden, D. J.; Ozkan, U. S. *J. Catal.* **2004**, *223*, 340–351.
(11) Águila, G.; Jiménez, J.; Guerrero, S.; Gracia, F.; Chornik, B.; Quinteros, S.; Araya, P. *Appl. Catal., A* **2009**, *360*, 98–105.
(12) Gunter, M. M.; Ressler, T.; Bems, B.; Buscher, C.; Genger, T.; Hinrichsen, O.; Muhler, M.; Schlogl, R. *Catal. Lett.* **2001**, *71*, 37–44.
(13) Baltes, C.; Vukojevic, S.; Schüth, F. *J. Catal.* **2008**, *258*, 334–344.
(14) Chen, L.-F.; Guo, P.-J.; Qiao, M.-H.; Yan, S.-R.; Li, H.-X.; Shen, W.; Xu, H.-L.; Fan, K.-N. *J. Catal.* **2008**, *257*, 172–180.
(15) Chang, F.-W.; Yang, H.-C.; Roselin, L. S.; Kuo, W.-Y. *Appl. Catal., A* **2006**, *304*, 30–39.
(16) Wang, Z.; Liu, Q.; Yu, J.; Wu, T.; Wang, G. *Appl. Catal., A* **2003**, *239*, 87–94.
(17) Guo, L.; Zhou, J.; Mao, J.; Guo, X.; Zhang, S. *Appl. Catal., A* **2009**, *367*, 93–98.
(18) Díaz, G.; Pérez-Hernández, R.; Gómez-Cortés, A.; Benaissa, M.; Mariscal, R.; Fierro, J. L. G. *J. Catal.* **1999**, *187*, 1–14.
(19) Bennici, S.; Gervasini, A.; Ravasio, N.; Zaccheria, F. *J. Phys. Chem. B* **2003**, *107*, 5168–5176.
(20) Avgouropoulos, G.; Ioannides, T. *Appl. Catal., B* **2006**, *67*, 1–11.
(21) Hughes, R. *Deactivation of Catalysts*; Academic Press: New York, 1984.
(22) Twigg, M. V.; Spencer, M. S. *Appl. Catal., A* **2001**, *212*, 161–174.
(23) Fixman, E. M.; Abello, M. C.; Gorriz, O. F.; Arrúa, L. A. *Appl. Catal., A* **2007**, *319*, 111–118.
(24) Huang, Z.; Cui, F.; Kang, H.; Chen, J.; Zhang, X.; Xia, C. *Chem. Mater.* **2008**, *20*, 5090–5099.
(25) Han, J. H.; Lee, S. W.; Choi, G.-J.; Lee, S. Y.; Hwang, C. S.; Dussarrat, C.; Gatineau, J. *Chem. Mater.* **2008**, *21*, 207–209.
(26) Lichtenegger, H. C.; Schoberl, T.; Bartl, M. H.; Waite, H.; Stucky, G. D. *Science* **2002**, *298*, 389–392.
(27) Lu, C.; Qi, L.; Yang, J.; Zhang, D.; Wu, N.; Ma, J. *J. Phys. Chem. B* **2004**, *108*, 17825–17831.
(28) Gao, X. P.; Bao, J. L.; Pan, G. L.; Zhu, H. Y.; Huang, P. X.; Wu, F.; Song, D. Y. *J. Phys. Chem. B* **2004**, *108*, 5547–5551.
(29) Anandan, S.; Wen, X.; Yang, S. *Mater. Chem. Phys.* **2005**, *93*, 35–40.
(30) Xiao, H.-M.; Zhu, L.-P.; Liu, X.-M.; Fu, S.-Y. *Solid State Commun.* **2007**, *141*, 431–435.
(31) Jenkins, R.; Snyder, R. L. *Introduction to X-ray Powder Diffractometry*; John Wiley & Sons: New York, 1996.
(32) Langford, J. I. *J. Appl. Crystallogr.* **1978**, *11*, 10–14.
(33) Günter, M. M.; Ressler, T.; Bems, B.; Büscher, C.; Genger, T.; Hinrichsen, O.; Muhler, M.; Schlögl, R. *Catal. Lett.* **2001**, *71*, 37–44.
(34) Toupance, T.; Kermarec, M.; Lambert, J.-F.; Louis, C. *J. Phys. Chem. B* **2002**, *106*, 2277–2286.
(35) Rodríguez-Clemente, R.; Serna, C. J.; Ocaña, M.; Matijevic, E. *J. Cryst. Growth* **1994**, *143*, 277–286.
(36) Liu, N.; Wu, D.; Wu, H.; Luo, F.; Chen, J. *Solid State Sci.* **2008**, *10*, 1049–1055.
(37) Toupance, T.; Kermarec, M.; Louis, C. *J. Phys. Chem. B* **2000**, *104*, 965–972.
(38) Nyquist, R. A.; Kagel, R. O. *Infrared Spectra of Inorganic Compounds*; Academic Press: New York, 1971.
(39) Wen, X. G.; Xie, Y. T.; Choi, C. L.; Wan, K. C.; Li, X. Y.; Yang, S. H. *Langmuir* **2005**, *21*, 4729–4737.
(40) Van Der Grift, C. J. G.; Elberse, P. A.; Mulder, A.; Geus, J. W. *Appl. Catal.* **1990**, *59*, 275–289.
(41) Zheng, M. F.; Zhao, T. B.; Xu, W. G.; Li, F. Y.; Wang, Y. *J. Mater. Sci.* **2007**, *42*, 8320–8325.
(42) Burattin, P.; Che, M.; Louis, C. *J. Phys. Chem. B* **1999**, *103*, 6171–6178.
(43) Marchi, A. J.; Fierro, J. L. G.; Santamaría, J.; Monzón, A. *Appl. Catal., A* **1996**, *142*, 375–386.
(44) Chary, K. V. R.; Seela, K. K.; Sagar, G. V.; Sreedhar, B. *J. Phys. Chem. B* **2004**, *108*, 658–663.
(45) Bond, G. C.; Namijo, S. N.; Wakeman, J. S. *J. Mol. Catal.* **1991**, *64*, 305–319.
(46) Chang, F.-W.; Kuo, W.-Y.; Lee, K.-C. *Appl. Catal., A* **2003**, *246*, 253–264.
(47) Guerreiro, E. D.; Gorriz, O. F.; Larsen, G.; Arrúa, L. A. *Appl. Catal., A* **2000**, *204*, 33–48.
(48) Auroux, A.; Gervasini, A.; Guimon, C. *J. Phys. Chem. B* **1999**, *103*, 7195–7205.
(49) Xu, Q.; Jia, G.; Zhang, J.; Feng, Z.; Li, C. *J. Phys. Chem. C* **2008**, *112*, 9387–9393.
(50) Burattin, P.; Che, M.; Louis, C. *J. Phys. Chem. B* **1997**, *101*, 7060–7074.
(51) Song, X.; Sun, S.; Zhang, W.; Yu, H.; Fan, W. *J. Phys. Chem. B* **2004**, *108*, 5200–5205.
(52) Wang, W.; Lan, C.; Li, Y.; Hong, K.; Wang, G. *Chem. Phys. Lett.* **2002**, *366*, 220–223.
(53) Du, G. H.; Van Tendeloo, G. *Chem. Phys. Lett.* **2004**, *393*, 64–69.
(54) Wen, X.; Zhang, W.; Yang, S. *Langmuir* **2003**, *19*, 5898–5903.
(55) Wen, X.; Zhang, W.; Yang, S.; Dai, Z. R.; Wang, Z. L. *Nano Lett.* **2002**, *2*, 1397–1401.
(56) Gao, P.; Zhang, M.; Niu, Z.; Xiao, Q. *Chem. Commun.* **2007**, 5197–5199.
(57) Durand-Keklikian, L.; Matijević, E. *Colloid Polym. Sci.* **1990**, *268*, 1151–1158.
(58) Sun, J. H.; Jia, Y. Z.; Jing, Y.; Yao, Y.; Li, W. *Russ. J. Inorg. Chem.* **2008**, *53*, 36–39.
(59) Singh, D. P.; Ojha, A. K.; Srivastava, O. N. *J. Phys. Chem. C* **2009**, *113*, 3409–3418.

JP101136X